Enhanced Friedel-Crafts Benzylation Activity of Bimetallic WSn-KIT-6 Catalysts

Rajamanickam Maheswari, Anand Ramanathan, Hongda Zhu, Aline Araújo do Nascimento Araújo, Clint Chapman, Yu Tang, Franklin (Feng) Tao, Bala Subramaniam

PII: S0021-9517(20)30275-X
DOI: https://doi.org/10.1016/j.jcat.2020.07.001
Reference: YJCAT 13813

To appear in: *Journal of Catalysis*

Received Date: 17 March 2020
Revised Date: 28 June 2020
Accepted Date: 2 July 2020

Please cite this article as: R. Maheswari, A. Ramanathan, H. Zhu, A. Araújo do Nascimento Araújo, C. Chapman, Y. Tang, F. (Feng) Tao, B. Subramaniam, Enhanced Friedel-Crafts Benzylation Activity of Bimetallic WSn-KIT-6 Catalysts, *Journal of Catalysis* (2020), doi: https://doi.org/10.1016/j.jcat.2020.07.001

Enhanced Friedel-Crafts Benzylation Activity of Bimetallic WSn-KIT-6 Catalysts

Rajamanickam Maheswari[a], Anand Ramanathan[a], Hongda Zhu [a,b], Aline Araújo do Nascimento Araújo[a], Clint Chapman,[b] Yu Tang,[a] Franklin (Feng) Tao[a] and Bala Subramaniam[a,b*]

[a]Center for Environmentally Beneficial Catalysis, The University of Kansas, Lawrence, KS 66047, USA

[b]Department of Chemical and Petroleum Engineering, The University of Kansas, Lawrence, KS 66045, USA

*Corresponding author. E-mail: bsubramaniam@ku.edu, Tel.: +1-785-864-2903; fax: +1-785-864-6051.

Abstract

A series of W and Sn-containing KIT-6 mesoporous silicates (designated as W_xSn_5) with similar Sn (~5 wt%) and varying W (x = 3 – 23 wt%) loadings were prepared by a one-pot hydrothermal synthesis method. No detectable bulk WO_3 species were observed for W loading up to 14 wt% with preferential dispersion of WO_x species near SnO_2 sites. The W_xSn_5 materials exhibited superior performance for Friedel-Crafts anisole benzylation with intrinsic rate constants for all W_xSn_5 catalysts being greater than those without Sn. Based on results from DR-UV-Vis, XRD, XPS, EXAFS techniques, we postulate that the W_xSn_5 materials contain both isolated WO_4/SnO_2 and isolated WO_4/SiO_2 as active species, with the former being more active. The relative populations of these two highly dispersed species dictate the overall catalyst activity. The intrinsic activities of the W_xSn_5 catalysts are found to scale linearly with total acidity but are mainly dictated by the Lewis acid sites.

Keywords: tungsten; tin; acidity; mesoporous; Friedel–Crafts benzylation

1. Introduction

The addition of tungsten to ZrO_2, SnO_2, TiO_2 and Fe_2O_3 creates solid superacids that are active for isomerization of butane, pentane and isopentane [1-3]. In the case of tungstated zirconia, the activity is related to the formation of subnanometer WO_x species incorporated with zirconium cations [4]. These supported metal oxides often possess a low surface area (< 50 m^2/g) and correspondingly low dispersion of WOx species. To increase the dispersion of active sites, it is desirable to support them in high surface area supports such as ordered mesoporous silicates (OMS). Other advantages of OMS materials include tunable pore size in a narrow distribution and synthesis using direct one-pot methods. In recent years, we have incorporated various mono and bimetallic combinations (such as W, Zr, Nb, WZr, WNb and WTi) into mesoporous silicates via one-pot hydrothermal synthesis methods [5-14]. For instance, W and Zr were incorporated in KIT-6 support and a synergistic effect was observed for dehydration of ethanol due to enhanced dispersion of W in the presence of isolated Zr^{4+} sites as well as on nanodomains of ZrO_2 [12]. Similarly, the introduction of Nb as either isolated sites or nanodomains of octahedral Nb_2O_5 resulted in the formation of new and more active sites, resulting in increased propene yield in the metathesis of ethylene and 2-butene [13]. A simple impregnation of Na_2WO_4 on Ti-TUD-1 was also reported to enhance catalytic activity during the esterification of acetic acid and *n*-butanol [14].

Recently, enhanced oxidation activity of WO_3/SnO_2 prepared by either co-precipitation or impregnation methods has been reported for the oxidation of 1,2-benzenedimethanol to phthalide by H_2O_2 [15]. The enhanced activity is attributed to the high dispersion of tungsten species on the support upon calcination with few W^{6+} ions incorporated into the SnO_2 lattice. MoO_3/SnO_2 and WO_3/SnO_2 prepared by impregnation method were also reported to be an effective catalyst for acetalization of glycerol [16]. Sn–W mixed oxide prepared by calcination of the Sn–W mixed hydroxide precursor has been reported to show a higher yield (39 – 70%) towards the synthesis of 5-hydroxymethylfurfural (HMF) from hexoses compared to Amberlyst-15 and H-mordenite catalysts [17]. The similar catalyst system has also been reported for the synthesis of glycerol carbonate from glycerol and urea exhibiting 52% glycerol conversion with >95% selectivity towards glycerol carbonate [18]. However, such catalysts are reported to deactivate during the transesterification of soybean oil with methanol [19]. Given that W-Sn mixed oxides are effective for both oxidation and acid catalyzed reactions, it is desirable to incorporate both W and Sn in KIT-6 support similar to WZr-KIT-6 and WNb-KIT-6 catalysts.

In this work, we extend the one-pot synthesis procedure to incorporate Sn and W into KIT-6 mesoporous silicate. Being a bulkier element compared to Zr and Nb, Sn forms predominantly isolated Sn^{4+} sites when incorporated in KIT-5 and KIT-6 silicates [10, 20] at a loading of <4 wt%. At much higher loadings (> 7 wt% Sn), bulky SnO_x particles with a broad distribution of sizes are formed. Hence, as previously shown, we chose a Sn loading of 5 wt% to form nano-domains of SnO_2 particles. The W precursor solution is added to the synthesis mixture after 24 h following the formation of the SnO_2 nanodomains, in order to maximize the dispersion and interaction of W with Sn species. The catalysts prepared in this manner are designated as W_xSn_y, where x and y denote the wt% of W and Sn, respectively, in the synthesis mixture.

The alkylation of anisole with benzyl alcohol is often used as a test reaction for catalysts containing Lewis and/or Brønsted acid sites (Scheme 1). For example, Lewis acidic γ-alumina [21] yields mainly dibenzyl ether (~32% yield), the condensation product of benzyl alcohol, at 160 °C after 5 h. On the other hand, Brønsted acidic zeolites such as ZSM-5 and beta zeolites require either higher reaction temperature (~170 °C) [22] or the presence of mesopores [23] to form benzylated anisoles. Hence, this reaction is ideal for investigating the performance of W_xSn_yKIT-6 materials that contain both Lewis and Brønsted acid sites, and probing possible synergistic effects. Herein, we present results of kinetic analysis showing that benzylation activity is enhanced in W_xSn_y materials (compared to Sn-free materials at identical W loadings). This is attributed to the enhanced dispersion of monomeric WO_x species on the catalyst surface as well as the formation of more active species, as evidenced by complementary catalyst characterization results from techniques such as X-ray absorption fine structure (XAS), X-ray photoelectron spectroscopy (XPS) and X-ray powder diffraction (XRD).

2. Experimental

2.1. Chemicals

Tri-block co-polymer (Pluronic P123, EO_{20}–PO_{70}–EO_{20}, with an average molecular weight of ~5,800, Aldrich), ammonium metatungstate [$(NH_4)_6H_2W_{12}O_{40}\cdot xH_2O$, Aldrich], Tin (IV) chloride pentahydrate (98%, Strem Chemicals), tetraethyl orthosilicate (TEOS) (98% Acros Organics) and hydrochloric acid (37%, Fisher) were used as received.

2.2. Synthesis of W and Sn containing mesoporous silicate (KIT-6)

In a typical synthesis procedure, 5 g of P123 were dissolved in 185 mL of 0.5 N hydrochloric acid solution under stirring at 35 °C. Then, 5 g of n-butanol were added and stirred for another 1 h. Following this step, 10.8 g TEOS and the required amount of $SnCl_4\cdot 5H_2O$ to yield 5 wt% Sn in the final solid was added. After stirring for 24 h at 35 °C, an appropriate quantity of ammonium metatungstate was added to yield final W wt% of 3, 9, 14 and 23. The mixture was stirred at 35 °C for 24 h and heated at 100 °C for another 24 h. The resulting precipitate was filtered, dried and calcined in flowing air at 550 °C for 5 h at a heating rate of 1.5 °C/min. The synthesized samples are denoted as W_xSn_y where x and y represent the wt% of W and Sn (y is either 0 or 5). The wt% of W and Sn measured by XRF in the prepared catalysts are given in Table 1. For catalytic activity comparison, monometallic W-KIT-6 (represented as $W_{14}Sn_0$) and Sn-KIT-6 (represented as W_0Sn_5) materials were also prepared as reported elsewhere [5, 10] employing ammonium metatungstate and stannic chloride as W and Sn sources, respectively.

2.3. Catalyst characterization

Small Angle X-ray Scattering (SAXS) and wide angle XRD patterns were recorded on a PANalytical Empyrean instrument with CuKα radiation in transmission and reflection modes operating at 45 kV and 40 mA, respectively. The bulk elemental composition of the powdered samples was determined using XRF (PANalytical Zetium) instrument. The specific surface area, pore volume and pore size distributions were calculated from the N_2 sorption isotherms measured at liquid N_2 temperature using a Quantachrome NOVA 2200e analyzer. Prior to the physisorption experiment, the samples were heated in vacuum at 200 °C for 1 h. The diffuse reflectance UV–vis spectra were collected on a Perkin Elmer Lambda 850 spectrophotometer equipped with a diffuse reflectance integrating sphere and Spectralon as the reference. Temperature programmed desorption of ammonia (NH_3-TPD) and temperature programmed reduction (H_2-TPR) profiles were obtained using a Micromeritics Autochem 2910 instrument. FTIR spectra of adsorbed pyridine were obtained on a Tensor-27 instrument with Pike diffuse reflectance accessory, as reported elsewhere [9]. The concentrations of Brønsted and Lewis sites were estimated from their respective bands at 1545 cm^{-1} and 1450 cm^{-1} by employing reported adsorption coefficients (0.078 cm μmol^{-1} for Brønsted acid sites and 0.165 cm $\mu mol^{-1}$for Lewis) [24].

EXAFS studies of W L_3 edge and Sn K edge were performed at beamline 2-2 at Stanford Synchrotron Radiation Laboratory in California, USA. The X-ray was monochoromated by Si (220) double crystal. The catalyst samples were pressed into round pellets (13 mm diameter and ~ 0.1 mm thickness) and mounted on the sample stage. The X-ray absorption signal was measured by gas ionic chamber detectors under transmission mode. The absorption spectrum of the corresponding metal foil reference was also collected and utilized as the energy calibration reference. The XAS data files were analyzed and fitted using the Demeter software package [25]. The amplitude factor S_0^2 was obtained by fitting the metal foil spectrum with full coordination in the 1st shell and used in subsequent data fitting wherein the coordination number, bond length and the Debye Waller factor were the fitted variables. The fitted k range was 3~12 $Å^{-1}$ and the fitted R range was 1~4 Å.

X-ray photoelectron spectroscopy (XPS) was measured on a PHI 5000 Versa Probe II instrument employing monochromated Al Kα (50 W, 15 kV) X-ray with a measurement spot size (beam diameter) of 200 μm. The charging effect was eliminated by a dual-beam charge neutralizer. The spherical capacitance analyzer was operated with a pass energy of 46.95 eV for detailed scan. Prior to the analysis, the surface of the catalyst was sputtered with Ar^+ ions (2.0 keV) for 5 min to expose the elements that reside deep in the pores of the catalyst. The following spectra were recorded: survey spectrum, Si 2p, Sn 3$d_{5/2}$, and W 4f. The resulting spectral data were processed by MultiPak software. The W 4f doublet splitting was constrained to 2.18 eV [26]. All XPS peaks were referenced to the Si 2p peak at 103.5 eV [27].

2.4. Friedel–Crafts benzylation of anisole with benzyl alcohol

Catalytic testing was performed in a 25 mL two-necked round bottom flask equipped with a magnetic stirrer and a reflux condenser. In a typical experiment, benzyl alcohol (1.08 g, 10 mmol) or dibenzylether (0.99 g, 5 mmol), anisole (10.8 g, 100 mmol), dodecane (0.34 g, 2 mmol, internal standard) and catalyst (100 mg) were charged into the reactor. The reaction mixture was heated to the desired temperature, typically 130 °C, while being mixed with a magnetic stirrer (1000 rpm). The headspace was blanketed with flowing N_2 (50 std cc/min) at 1 atm and the reaction was carried out for 2 h. A small volume (100 μL) of the reaction mixture was periodically sampled and analyzed with a Varian CP-3800 gas chromatograph equipped with a ZB-Wax capillary column (25 m × 0.32 mm × 0.2 μm) and a flame-ionization detector. The C balance, based on analysis of the reactants and liquid phase products was 100 ± 3%.

The following definitions for substrate conversion (X_{sub}) and selectivities (S_i for product i) are used to evaluate the performance of the various catalysts, including W_xSn_y.

$$X_{\mathrm{s}} = \frac{n_{\mathrm{s},0} - n_{\mathrm{s}}}{n_{\mathrm{s},0}} \times 100\% \qquad (1)$$

$$S_i = \frac{n_i}{n_{\mathrm{sub},0} - n_{\mathrm{sub}}} \times 100\% \qquad (2)$$

where $n_{\mathrm{s},0}$ [mol] represents the initial moles of the limiting substrate (benzyl alcohol or dibenzyl ether) while n_{s} and n_i [mol] represent the moles of the limiting substrate and products in the reaction mixture at a given reaction time, respectively.

The turnover frequency (TOF_0) is calculated using the following equations based on the conversion of the limiting substrate.

$$TOF = \frac{m_{\mathrm{s},0}}{m_{\mathrm{c}} M_{\mathrm{s}} \Sigma\left({}^{x_{\mathrm{m}}}/_{M_{\mathrm{m}}}\right)} X_i'\left(t \rightarrow 0^+\right) \qquad (3)$$

where $m_{\mathrm{s},0}$ [g] is the initial mass of the limiting substrate (benzyl alcohol or dibenzyl ether), m_{c} [g] is the mass of catalyst, x_{m} is the mass fraction of W, Nb or Zr in the catalyst, M_{m} and M_{s} are the molecular weights of the metal (W, Nb, Sn or Zr) and limiting substrate, respectively, and X' (t) is the initial slope of the substrate conversion vs time profile, where the conversion range is <

20%, estimated with MATLAB R2016a software. It must be noted that since the Sn content in the W_xSn_yKIT-6 catalysts is constant, the TOF values are reflective of the changes in the W content in the bimetallic catalysts. Further, under our reaction conditions, mass transfer limitations are insignificant (see ESI for calculations).

To probe the reaction pathways further and to compare the decoupled reaction rates on materials with various metal loadings, reactions using W_xSn_0 and W_xSn_5 materials were carried out at 110 °C, such that the relatively slower reactions allow kinetic modeling with finite conversion during 20 – 40 min runs. The temporal solutions to the ordinary differential equations (ODEs) describing a stirred batch reactor model containing reaction rate expressions were fit to the substrate and product concentrations estimated from GC results.

$$\frac{\mathrm{d}c_i}{\mathrm{d}t} = r_i$$

where c_i is the concentration of species i, r_i is the net formation rate of species i. Several sets of rate expressions were derived from possible reaction pathways, as discussed in detail in section 3.2 and the ESI.

3. Results and discussion

3.1. Characterization of W_xSn_y Catalysts

Figure 1 shows the XRD patterns of W_xSn_5 compared with W-KIT-6 ($W_{14}Sn_0$) and Sn-KIT-6 (W_0Sn_5) samples. All W_xSn_5 materials show well defined reflections of SnO_2 (ICSD 98-016-9032) that clearly become narrower with increasing W content. The average crystallite sizes, estimated from the Debye–Sherrer equation, are 5, 6.8, 8.8, 11.6 and 53 nm, respectively, for W_0Sn_5, W_3Sn_5, W_9Sn_5, $W_{14}Sn_5$ and $W_{23}Sn_5$ materials. At the maximum W loading of 23 wt%, intense peaks characteristic of crystalline WO_3 (ICSD 98-003-6168) are observed. Interestingly, XRD reflections characteristic of WO_3 are not observed in other W_xSn_5 catalysts, even at the relatively high W loadings in $W_{14}Sn_5$. This may indicate the presence of highly dispersed WO_x species and/or amorphous WO_x nanoclusters that are < 3 nm, the lower detection limit of the instrument. However, EXAFS results (discussed later) rule out the presence of WO_3 nanoclusters in the $W_{14}Sn_5$ materials. Interestingly, when using Na_2WO_4 as the W source (instead of ammonium metatungstate used in the present study), crystalline tungsten oxide nanoclusters are reported to form on silicates (KIT-6, KIT-5 and SBA-16) at approximately 12 wt% W loadings [5, 28, 29].

Nitrogen adsorption isotherms of W_xSn_5 samples along with pore size distributions are shown in Figure 2. All the bimetallic catalyst formulations exhibit Type IV isotherm with a H1 hysteresis loop characteristic of mesoporous materials containing large mesopores [30]. Table 1 lists the physicochemical characteristics of W_xSn_y catalysts. For tungsten loadings up to 14 wt%, the surface areas and pore volumes decrease while being in the ranges of 585 – 712 m^2/g and pore 0.73 – 0.98 cm^3/g, respectively. The corresponding pore size distributions are narrowly centered at approximately 9.2 nm. However, a further increase in the W loading to 23 wt% leads to a significant decrease in surface area and pore volume to 411 m^2/g to 0.51 cm^3/g, respectively. This decrease may result from the formation of nanoclusters of bulk oxides of tin and tungsten within the pores, as also borne out by the XRD patterns at a W loading of 23 wt% (Fig. 1).

Representative TEM images (Figure 3a) of the $W_{14}Sn_5$ sample reveal uniform hexagonal mesopores. In addition, crystallites and aggregates of SnO_2 particles, ranging in sizes between 20 and 100 nm, appear to be distributed throughout the silicate network as evidenced from TEM image (Figure 3a) and High-Angle Annular Dark-Field (HAADF) STEM images (Figure 3b). The presence of nanocrystalline SnO_2 is consistent with wide angle XRD spectra (Figure 1).

EDX elemental mapping data clearly show that the W species are preferentially distributed on Sn species (Figure 3c-f). Further, the surface elemental composition was also probed on a larger area (scale bar 20 μm) by scanned X-ray images (SXI) images. The XPS mapping revealed a homogenous distribution of W and Sn species in the silica matrix (see Figure S1).

Figure 4 summarizes the SAXS pattern of W_xSn_5 samples. As reported for other metal incorporated KIT-6 silicates [5, 7, 9, 10], a characteristic intense reflection peak due to the (211) plane and a distinct (220) plane of *Ia3d* space group are observed. The (211) peak becomes progressively weaker and broader at higher W loadings, indicative of a decrease in the mesostructured ordering.

Diffuse reflectance UV-Vis spectra (Figure S2) of the Sn-KIT-6 (W_0Sn_5) sample (Fig. S2, e) shows an unresolved broad absorption band with inflections at 210 and 270 nm. The band around 210 nm is attributed to ligand-to-metal charge transfer from an O^{2-} to an isolated Sn^{4+} in a tetrahedral configuration. Hexa-coordinated polymeric Sn–O–Sn-type species (detected in wide angle XRD and TEM images) are typically observed around 270 nm [31, 32]. W_xSn_5 samples (Fig. S2, a-d) show an absorption peak between 227 and 235 nm that increases with W loading up to ~9 wt% W and decreases slightly with a further increase in W loading, indicating that this peak represents the intrinsic nature of W coordination in the W_xSn_5 samples. The band around 227-235 nm is generally attributed to isolated $[WO_4]^{2-}$ species [33]. The shoulder peaks that are evident between 250–270 nm at the highest W loading in $W_{23}Sn_5$ (Fig. S2, d) and in tungsten-only ($W_{14}Sn_0$; Fig. S2, f) samples are attributed to octahedral polytungstate species [5, 8, 23, 33].

Temperature-programmed desorption of ammonia (NH_3-TPD, Figure S3) profiles of Sn-KIT-6 (Figure. S3, e) show a weak and broad peak centered around 300 °C with a relatively low acidity of 0.04 mmol NH_3/g (Table 1). The total acidity increases with W loading in W_xSn_5

materials (Fig. S3, a–d), with a sharp increase from 0.09 to 0.50 mmol NH_3/g when the W content is increased from 3 to 14 wt%. However, a further increase in W loading from 14 to 23 wt% resulted in only a marginal increase in acidity by 0.06 mmol NH_3/g (Table 1). This implies that the crystallite WO_3 sites observed from XRD (Figure 1) are weakly acidic. Interestingly, despite their similar W contents, the total acidity of W-KIT-6 ($W_{14}Sn_0$) (0.31 mmol NH_3/g) is significantly lower than that of $W_{14}Sn_5$ (0.50 mmol NH_3/g). These findings suggest that the interactions between W and Sn species in W_xSn_5 samples may be enhancing catalyst acidity.

Figure 5 shows the FT-IR spectra of adsorbed pyridine species over W_xSn_y catalysts measured at 100 °C. The relative ratios of Lewis (L) and Brønsted (B) sites are given in Table 1. The presence of Brønsted sites protonates the pyridine molecule resulting in their adsorption as pyridinium ions observed around 1545 cm^{-1} whereas coordinatively bound pyridine on Lewis acid sites are observed at 1450 cm^{-1} [21]. As seen from the spectra in Figure 5, Sn-KIT-6 (W_0Sn_5) and W_3Sn_5 samples display very little if any Brønsted acid sites, while all the other materials exhibit Brønsted acidity that increases significantly with W loading. In contrast, all the materials possess Lewis acidity which is less sensitive to metal loading. In combination with NH_3-TPD, it can be inferred that $W_{23}Sn_5$ and $W_{14}Sn_5$ materials possess more acid sites and increased acidity compared to $W_{14}Sn_0$ (W-KIT-6) sample.

Temperature programmed reduction (H_2-TPR, Figure S4) profiles of Sn-KIT-6 (W_0Sn_5) show gradual H_2 consumption up to 415 °C followed by broad and distinct reduction peaks occurring between 440 and 620 °C. Usually a bulk SnO_2 reduction happens around 760 °C [34, 35] and the lack of such peak clearly indicates the presence of isolated sites of tin oxide nanoparticles that get reduced around 550 °C[35]. In the case of W_xSn_5 catalysts, this peak is progressively shifted to higher temperatures (602, 625, 714 and 735 °C, respectively) with increasing W content (3, 9, 14 and 23 wt%). We attribute this increase in the SnO_2 reduction temperatures to either strong interaction with WO_x species and/or an increase in the size of the SnO_2 particles (evidenced in XRD). The W-KIT-6 ($W_{14}Sn_0$) material shows two broad reduction peaks one around 804 °C and the other around 990 °C due to the stepwise reduction of $W^{6+} \rightarrow W^{4+}$ and $W^{4+} \rightarrow W^0$, respectively [16, 28, 29]. Further, the progressive shift of the WO_x reduction peak in W_xSn_5 materials to higher temperatures indicates possible interactions between the WO_x and SnO_x species at the higher W loadings.

3.2. Friedel-Crafts benzylation of anisole

As shown in Scheme 1, the Friedel-Crafts benzylation of anisole with benzyl alcohol over W_xSn_5 catalysts results in the formation of *ortho*-benzylated anisole (*o*-BA), *para*-benzylated anisole (*p*-BA) and dibenzyl ether (DBE). It has been reported that the self-etherification step of benzyl alcohol leading to the formation of the DBE is faster than the alkylation reaction [21, 36, 37]. However, DBE also acts as an alkylating agent and gets eventually consumed at longer reaction times to produce the benzylated products [38].

Figure 6a compares the temporal BzOH conversion profiles of W_xSn_5 catalysts with monometallic $W_{14}Sn_0$ (W-KIT-6) and W_0Sn_5 (Sn-KIT-6) catalysts for the benzylation of anisole at similar operating conditions (130 °C). The temporal product distribution obtained with the different catalysts is given in Table 2. W_0Sn_5 (Sn only) showed < 9% BzOH conversion after 2 h with DBE as the main product (> 95%, Table 2, Entry 2). In contrast, W_xSn_5 materials show significant BzOH conversion. While approximately 30% BzOH conversion was observed over W_3Sn_5 catalyst in 2 h (Table 2, Entry 3), nearly complete BzOH conversion was achieved in less than 30 min over $W_{14}Sn_5$ catalyst (Table 2, Entry 5). As the W loading was increased to 23%

($W_{23}Sn_5$), a moderate decrease in the BzOH conversion rate was observed (Fig. 6a and Table 2, Entry 7).

The TOFs computed from the linear portion of the temporal conversion curves show that Sn-based silicate provides relatively low TOF of 0.14 min^{-1} (Table 2, Entry 2). In contrast, the TOFs are greater when W is present, increasing by more than an order of magnitude as the W loading is increased from 3 wt% (TOF = 0.26 min^{-1}) to 14 wt% (TOF = 11.07 min^{-1}). Interestingly, the TOF for the $W_{14}Sn_0$ catalyst without Sn (TOF = 3.53 min^{-1}; Table 2, Entry 6) is approximately three times lower than the $W_{14}Sn_5$ catalyst at similar W loading (TOF = 11.07 min^{-1}; Table 2, Entry 5).

The temporal product distribution reveals significant differences in the product selectivity among the various catalysts. Even though the $W_{14}Sn_0$ catalyst shows facile BzOH conversion, it mainly forms DBE (~80%) after 20 min and with time, DBE reacts with anisole yielding benzylanisoles. Yet nearly 15% DBE remains unconverted after 60 min (Table 2, Entry 6). In sharp contrast, $W_{14}Sn_5$ catalyst shows only ~20% DBE selectivity after 10 min and the reaction is complete after 30 min forming only the ring alkylated products, *o*-BA and *p*-BA (Table 2, Entry 5).

As shown in Table S1, various other monometal-incorporated mesoporous silicates such as Zr-KIT-5 (Entry 1), Zr-KIT-6 (Entries 2–4), Nb-KIT-6 (Entries 5–7) showed generally lower conversion rates and higher DBE formation compared to the bimetallic W_xSn_5 catalysts (Table 2). In addition, the TOFs for these monometallic silicates (ranging from 0.11 min^{-1} to 2.18 min^{-1}) are several-fold lower compared to the maximum TOF value observed with the $W_{14}Sn_5$ catalyst (TOF = 11.07 min^{-1}, Table 2, Entry 5). These results clearly divulge the beneficial role of Sn in significantly enhancing W utilization in the mixed metal oxide (W_xSn_y) catalysts.

To probe the reaction pathway further, DBE was tested as an alkylating agent. The temporal DBE conversion profiles over W_xSn_5 catalysts are depicted in Figure 6b. The product distribution along with the TOFs are given in Table 3. As expected, the major products are o-BA and p-BA. As with BzOH as alkylating agent, the TOFs for W_xSn_5 catalysts display a maximum at a W loading of 14 wt% (TOF = 1.96 min^{-1}, Table 3, Entry 3) which is greater than the value (1.62 min^{-1}) observed with W-KIT-6 catalyst with similar W loading ($W_{14}Sn_0$; Table 3, Entry 1). However, the TOFs are much lower than those observed with BzOH as the benzylating agent suggesting that over W_xSn_y catalysts, the direct alkylation pathway involving BzOH is much faster (Scheme 1).

To decouple the kinetics of competing reactions of BzOH condensation and alkylation, several kinetic models (Scheme S1 and Equation Sets S6 – S10 in the ESI) were fitted to the experimental data acquired at 110 °C. The W_3Sn_0 sample show negligible activity during the 40 minutes run and was therefore excluded from the kinetic modeling. Also, on the relatively more active materials, $W_{14}Sn_5$, $W_{23}Sn_0$, and $W_{23}Sn_5$, DBE forms predominantly benzylanisoles, resulting in the apparent rate constants being zero for BzOH formation from DBE, suggesting that DBE alkylation and DBE hydrolysis may share a common surface species produced by the rate-determining step, DBE adsorption. The best-fitting reaction scheme is as shown in Scheme 2, corresponding to the rate expressions Eq. 4a – 4c for the net formation rates of the species ($r_i = \frac{\mathrm{d}c_i}{\mathrm{d}t}$). The model confirms (a) the BzOH condensation is reversible, and (b) one mole of DBE reacts with two moles of anisole without forming free BzOH in the bulk liquid phase. The inclusion of water concentration into the hydrolysis of DBE deteriorated the fitting quality, suggesting that the adsorption of BzOH and DBE was likely the rate determining step for BzOH condensation and DBE hydrolysis, respectively.

$$r(\mathrm{BzOH}) = k_{-1}[\mathrm{DBE}] - k_1[\mathrm{BzOH}]^2 - k_2[\mathrm{BzOH}] \tag{4a}$$

$$r(\mathrm{DBE}) = -\frac{1}{2}k_{-1}[\mathrm{DBE}] + \frac{1}{2}k_1[\mathrm{BzOH}]^2 - k_3[\mathrm{DBE}] \tag{4b}$$

$$r(\mathrm{BA}) = k_2[\mathrm{BzOH}] + 2k_3[\mathrm{DBE}] \tag{4c}$$

The intrinsic rate constants obtained using the foregoing model were compared for catalysts with 5% Sn (W_xSn_5 catalysts) and without any Sn content (W_xSn_0 catalysts) at identical W loadings and operating temperature (Table 4). This comparison clearly shows that the intrinsic rate constants (any k value) are greater in the case of Sn-containing (W_xSn_5) catalysts, providing compelling evidence for the beneficial role of Sn. Further, based on a linear-dependence analysis of the reaction rates at 130 °C and 110 °C against Lewis, Brønsted and total acid amounts (Figures S6 and S7), it is concluded that the observed activity is mainly dictated by the Lewis acid sites.

The reusability of $W_{14}Sn_5$ catalysts was also investigated. Following a reaction run, the catalyst was filtered, washed with acetonitrile, dried and calcined at 550 °C prior to its use in the next run. The nearly overlapping temporal conversion profiles (Figure S8) suggest that the active sites are preserved even after three reuses. This implies that insights gained into the active sites from catalyst characterization (such as EXAFS) with used catalysts are useful.

3.3. Nature of active species

The activity enhancement displayed by the W_xSn_5 catalysts correlates well with an increase in the number and nature of acid sites (Figures. S3 and 5) compared to the W_xSn_0 samples. Such increase could partially be attributed to the formation of isolated $[WO_4]^{2-}$ species as evidenced by EXAFS results. The presence of tin oxide could modify the chemical environment around the

WO_x species in a manner similar to recently reported metal dopants such as Zr, Nb, Hf, and Ta [12, 13], resulting in enhanced activity.

As a bulk characterization technique, XAS reveals the local coordination environment of target element atoms. All the target atoms in the sample contribute to the overall XAS signal. EXAFS of three spent catalysts (after runs at 130 °C) including $W_{14}Sn_0$, W_0Sn_5 and $W_{14}Sn_5$ were investigated to examine the coordination environment. The results of least-square fits in the *r-space* spectra are given in Table 5. Figure 7a represents the experimental data of the *r*-space of Sn-K edge (black line) of W_0Sn_5 and its fitted curve (red line). For the spent W_0Sn_5 catalyst (Sn-KIT-6), the coordination number of O to Sn in the first shell is 6.24 with an average Sn–O distance of 2.04 Å (Table 5). The CN(Sn–O) of 6.24 is consistent with the ideal number of oxygen atoms around a Sn atom in bulk SnO_2 crystal [39]. The second shell could be interpreted by two types of Sn atoms, Sn^{α} and Sn^{β} which are reflected by two separated peaks as marked in the *r*-space (Figure 7a). The fitting and analysis of the *r*-space suggest that the coordination numbers of Sn^{α} and Sn^{β} to the center Sn atom are 1.74 and 5.44, respectively. Clearly, these EXAFS results suggest the formation of SnO_2 nanoclusters, which is also supported by the XRD pattern of W_0Sn_5 in Figure 1.

The experimental and fitted curves of W-L_3 edge of $W_{14}Sn_0$ are shown as black and red lines (Figure 7b), respectively. The peak centered at 1.3 Å stems from two different types of oxygen atoms which coordinate with the central W atoms with distances of 1.797 and 2.410 Å. The two peaks at 2.6 and 3.2 Å were assigned to Si and W atoms in the second shells of the central W atom. The distances from the Si and W atoms to the central W atoms are 3.384 and 3.82 Å, respectively, and are consistent with literature reports [40-43].

Figure 7c presents the experimental (black) and fit (red) *r*-space of Sn-K edge of $W_{14}Sn_5$. Similar to W_0Sn_5, the Sn atoms were identified in both the first and second shells in the *r*-space spectrum suggesting the existence of SnO_2 nanoclusters in $W_{14}Sn_5$. However, Sn-(O)-W coordination is hard to be deconvoluted in the Sn K edge spectrum. This is because the XAS is a bulk measurement technique and hence the overall Sn K edge spectrum cannot sensitively capture the signal from a relatively small portion of Sn atoms potentially coordinated in the form of Sn-(O)-W. Further, from the XRD pattern of W_xSn_5 samples, it is evident that Sn exists as SnO_2 and crystalline WO_3 is evident only in the $W_{23}Sn_5$ sample (Figure 1). Hence, the formation of tin tungstate ($SnWO_4$) is excluded. Figure 7d represents the *r*-space of W-L_3 edge of $W_{14}Sn_5$. The *r*-space was deconvoluted into three peaks including a W–O of the first shell and W–(O)–Si and W–(O)–Sn in the second shell (Figure 7d). The W atoms in $W_{14}Sn_5$ most likely form WO_x monomer species on the surface of the mesopores. These WO_x monomer species are linked via W-O-Si bonds with the SiO_2 surface in the pores and via W-O-Sn bonds on the SnO_2 nano-domains.

Based on the foregoing discussion, a catalyst model and probable geometries of tungsten coordination with SiO_2 and SnO_2 are presented in Figures 8a and 8b, respectively. In this postulated model, SnO_x species exist in the form of nanoclusters/nanoparticles on the SiO_2 support while the W species are dispersed as even smaller particles on the surfaces of SnO_x and the SiO_2 support. Hence, the number of Sn atoms at the Sn-O-W interface is a relatively small fraction of the total Sn atoms. On the other hand, W is highly dispersed, resulting in a high fraction of W atoms at both the Sn-O-W and Si-O-W interfaces. Thus, while the Sn-O-W coordination is easily visible in W L3 edge EXAFS spectra, it is hard to distinguish in the Sn K edge EXAFS spectra. The increased TOF of W_xSn_y catalysts suggests that the WO_x species associated with Sn species enhances catalysis.

Compared to bulk techniques such as XAS and XRD, XPS provides more surface sensitive chemical information of the $W_{14}Sn_5$ catalyst (Figure S5). The photoemission feature of W 4*f* (31 – 42 eV) appears as a well resolved doublet attributed to W $4f_{7/2}$ and W $4f_{5/2}$ components [44, 45]. The peaks at lower binding energies (BE), 34.70 and 36.88 eV can be attributed to W–O–Si interactions, whereas those at higher BE, 37.52 and 39.70 eV are due to either W–O–W or W–O–Sn [46]. Since XAS studies suggest that there are two types of W atoms based on the average coordination number of O atoms around a W atom, we assign the peaks at higher BE to W–O–Sn interactions. Further, the spectra of Sn $3d_{5/2}$ could be deconvoluted to two components, which is assigned to two Sn chemical states viz., Sn-O-Sn and Sn-O-W. Thus, the XPS results complement XAS analysis and provide credence for the postulated catalyst structure (Figures 8a and 8b).

The catalyst model, supported by EXAFS, XPS and XRD results, suggests that the overall activity of the W_xSn_yKIT-6 catalysts is dictated by the relative populations of isolated W-O-Sn and isolated W-O-Si species (Figure 8b). From Table 4, it is clear that at identical W loadings, the intrinsic rate constants obtained with catalysts containing 5% Sn are greater than those without Sn. This implies that the W-O-Sn species are more active than the W-O-Si species.

4. Conclusions

We demonstrate that highly dispersed WO_x species can be generated by consecutive additions of Sn and W sources during the one-pot synthesis of KIT-6. Based on complementary catalyst characterization results (Diffuse Reflectance UV-Vis, XRD, XPS, EXAFS), we postulate that the overall activity of the W_xSn_yKIT-6 catalysts in the Friedel-Crafts benzylation of anisole is dictated by the relative populations of the W-O-Sn and W-O-Si species. At identical W loadings, the intrinsic rate constants obtained with catalysts containing 5% Sn are greater than those without Sn, implying that the W-O-Sn species are more active than the W-O-Si species. The intrinsic activity correlates linearly with total acidity but is mainly dictated by the Lewis acid sites. By facilitating the selective formation of the active W species (isolated WO_x species, with strong interaction with the Sn dopants), Sn doping enhances W utilization. These findings open new avenues for better understanding and exploiting bimetallic mesoporous silicates in various chemistries.

Acknowledgments

This research was supported from joint National Science Foundation and Environmental Protection Agency program Networks for Sustainable Material Synthesis and Design (NSF-EPA 1339661). The authors thank Dr. Prem Thapa of the Microscopy and Analytical Imaging Laboratory, University of Kansas for TEM characterizations. Use of the Stanford Synchrotron Radiation Light Source, SLAC National Accelerator Laboratory, is supported by the U.S. Department of Energy, Office of Science, Office of Basic Energy Sciences under Contract No. DE-AC02-76SF00515.

References

[1] M. Hino, K. Arata, Synthesis of solid superacid of tungsten oxide supported on zirconia and its catalytic action for reactions of butane and pentane, Journal of the Chemical Society, Chemical Communications, (1988) 1259-1260.

[2] M. Hino, K. Arata, Synthesis of Highly Acidic Catalysts of Tungsten Oxide Supported on Tin Oxide, Titanium Oxide, and Iron Oxide, Bulletin of the Chemical Society of Japan, 67 (1994) 1472-1474.

[3] S. Kuba, P. Lukinskas, R.K. Grasselli, B.C. Gates, H. Knözinger, Structure and properties of tungstated zirconia catalysts for alkane conversion, Journal of Catalysis, 216 (2003) 353-361.

[4] W. Zhou, E.I. Ross-Medgaarden, W.V. Knowles, M.S. Wong, I.E. Wachs, C.J. Kiely, Identification of active Zr–WO_x clusters on a ZrO_2 support for solid acid catalysts, Nature Chemistry, 1 (2009) 722-728.

[5] A. Ramanathan, B. Subramaniam, D. Badloe, U. Hanefeld, R. Maheswari, Direct incorporation of tungsten into ultra-large-pore three-dimensional mesoporous silicate framework: W-KIT-6, J. Porous Mater., 19 (2012) 961-968.

[6] Q. Pan, A. Ramanathan, W.K. Snavely, R.V. Chaudhari, B. Subramaniam, Synthesis and Dehydration Activity of Novel Lewis Acidic Ordered Mesoporous Silicate: Zr-KIT-6, Industrial & Engineering Chemistry Research, 52 (2013) 15481-15487.

[7] A. Ramanathan, B. Subramaniam, R. Maheswari, U. Hanefeld, Synthesis and characterization of Zirconium incorporated ultra large pore mesoporous silicate, Zr–KIT-6, Microporous and Mesoporous Materials, 167 (2013) 207-212.

[8] Q. Pan, A. Ramanathan, W.K. Snavely, R. Chaudhari, B. Subramaniam, Intrinsic Kinetics of Ethanol Dehydration Over Lewis Acidic Ordered Mesoporous Silicate, Zr-KIT-6, Topics in Catalysis, (2014) 1-5.

[9] A. Ramanathan, R. Maheswari, D.H. Barich, B. Subramaniam, Niobium incorporated mesoporous silicate, Nb-KIT-6: Synthesis and characterization, Microporous and Mesoporous Materials, 190 (2014) 240-247.

[10] R. Rajalakshmi, R. Maheswari, A. Ramanathan, Characterization and activity of novel tin incorporated ordered cubic mesoporous silicate, Sn-KIT-6, Materials Research Bulletin, 75 (2016) 224-229.

[11] H. Zhu, R.V. Chaudhari, B. Subramaniam, A. Ramanathan, J.-F. Wu, Effects of tunable acidity and basicity of Nb-KIT-6 catalysts on ethanol conversion: Experiments and kinetic modeling, AIChE Journal, 63 (2017) 2888-2899.

[12] H. Zhu, A. Ramanathan, J.-F. Wu, B. Subramaniam, Genesis of Strong Brønsted Acid Sites in WZr-KIT-6 Catalysts and Enhancement of Ethanol Dehydration Activity, ACS Catalysis, 8 (2018) 4848-4859.

[13] J.-F. Wu, A. Ramanathan, R. Kersting, A. Jystad, H. Zhu, Y. Hu, C.P. Marshall, M. Caricato, B. Subramaniam, Enhanced Olefin Metathesis Performance of Tungsten and Niobium Incorporated Bimetallic Silicates: Evidence of Synergistic Effects, ChemCatChem, doi: 10.1002/cctc.201902131 (2020).

[14] M.P. Pachamuthu, R. Maheswari, A. Ramanathan, Synthesis and characterizations of isolated WO4 anchored on mesoporous TiTUD-1 support, Applied Surface Science, 402 (2017) 286-293.

[15] Z. Zhang, Q. Zhu, J. Ding, X. Liu, W.-L. Dai, Effect of calcination temperature of the support and the catalyst of WO3/SnO2 on the catalytic oxidation of 1,2-benzenedimethanol by H2O2, Applied Catalysis A: General, 482 (2014) 171-178.

[16] B. Mallesham, P. Sudarsanam, G. Raju, B.M. Reddy, Design of highly efficient Mo and W-promoted SnO2 solid acids for heterogeneous catalysis: acetalization of bio-glycerol, Green Chemistry, 15 (2013) 478-489.

[17] K. Yamaguchi, T. Sakurada, Y. Ogasawara, N. Mizuno, Tin–Tungsten Mixed Oxide as Efficient Heterogeneous Catalyst for Conversion of Saccharides to Furan Derivatives, Chemistry Letters, 40 (2011) 542-543.

[18] K. Jagadeeswaraiah, C.R. Kumar, P.S.S. Prasad, S. Loridant, N. Lingaiah, Synthesis of glycerol carbonate from glycerol and urea over tin-tungsten mixed oxide catalysts, Applied Catalysis A: General, 469 (2014) 165-172.

[19] W. Xie, T. Wang, Biodiesel production from soybean oil transesterification using tin oxide-supported WO_3 catalysts, Fuel Processing Technology, 109 (2013) 150-155.

[20] R. Rajalakshmi, V.V. Srinivasan, M.P. Pachamuthu, R. Maheswari, Characterizations of tin (SnO_2) doped KIT-5 by direct synthesis, Materials Chemistry and Physics, 154 (2015) 164-169.

[21] M.H.C. de la Cruz, M.A. Abdel-Rehim, A.S. Rocha, J.F.C. da Silva, A. da Costa Faro, E.R. Lachter, Liquid phase alkylation of anisole by benzyl alcohol catalyzed on alumina-supported niobia, Catal. Commun., 8 (2007) 1650-1654.

[22] H. Jin, M.B. Ansari, E.-Y. Jeong, S.-E. Park, Effect of mesoporosity on selective benzylation of aromatics with benzyl alcohol over mesoporous ZSM-5, Journal of Catalysis, 291 (2012) 55-62.

[23] Z. Miao, H. Song, H. Zhao, L. Xu, L. Chou, One-pot synthesis of mesoporous ZrPW solid acid catalyst for liquid phase benzylation of anisole, Catalysis Science & Technology, 4 (2014) 838-850.

[24] J. Datka, B. Gil, A. Kubacka, Heterogeneity of OH groups in NaH-mordenites: Effect of Na/H exchange degree, Zeolites, 18 (1997) 245-249.

[25] B. Ravel, M. Newville, ATHENA, ARTEMIS, HEPHAESTUS: data analysis for X-ray absorption spectroscopy using IFEFFIT, Journal of Synchrotron Radiation, 12 (2005) 537-541.

[26] J.F. Moulder, W.F. Stickle, P.E. Sobol, K.D. Bomben, Handbook of X-ray Photoelectron Spectroscopy: A Reference Book of Standard Spectra for Identification and Interpretation of XPS Data, Perkin-Elmer Coporation, Eden Prairie, MN, 1992.

[27] NIST X-ray Photoelectron Spectroscopy Database, in, National Institute of Standards and Technology, Gaithersburg, MD.

[28] R. Maheswari, M.P. Pachamuthu, A. Ramanathan, B. Subramaniam, Synthesis, Characterization, and Epoxidation Activity of Tungsten-Incorporated SBA-16 (W-SBA-16), Industrial & Engineering Chemistry Research, 53 (2014) 18833-18839.

[29] A. Ramanathan, R. Maheswari, B.P. Grady, D.S. Moore, D.H. Barich, B. Subramaniam, Tungsten-incorporated cage-type mesoporous silicate: W-KIT-5, Microporous and Mesoporous Materials, 175 (2013) 43-49.

[30] M. Thommes, K. Kaneko, A.V. Neimark, J.P. Olivier, F. Rodriguez-Reinoso, J. Rouquerol, K.S.W. Sing, Physisorption of gases, with special reference to the evaluation of surface area and pore size distribution (IUPAC Technical Report), Pure and Applied Chemistry, 87 (2015) 1051.

[31] Z.C. Liu, H.R. Chen, W.M. Huang, J.L. Gu, W.B. Bu, Z.L. Hua, J.L. Shi, Synthesis of a new SnO_2/mesoporous silica composite with room-temperature photoluminescence, Microporous and Mesoporous Materials, 89 (2006) 270-275.

[32] S.-Y. Chen, H.-D. Tsai, W.-T. Chuang, J.-J. Lee, C.-Y. Tang, C.-Y. Lin, S. Cheng, Direct Preparation of Thermally Stable Sn-Incorporated SBA-15 Mesoporous Materials in the Self-Generated Acidic Environment, The Journal of Physical Chemistry C, 113 (2009) 15226-15238.

[33] Q. Zhao, S.-L. Chen, J. Gao, C. Xu, Effect of tungsten oxide loading on metathesis activity of ethene and 2-butene over WO_3/SiO_2 catalysts, Transition Met. Chem., 34 (2009) 621-627.

[34] X. Wang, Y.-c. Xie, Preparation and Characterization of SnO2-Based Composite Metal Oxides: Active and Thermally Stable Catalysts for CH4 Oxidation, Catalysis Letters, 75 (2001) 73-80.

[35] E.A. Alarcón, A.L. Villa, C.M.d. Correa, Characterization of Sn- and Zn-loaded MCM-41 catalysts for nopol synthesis, Microporous and Mesoporous Materials, 122 (2009) 208-215.

[36] A.B. Deshpande, A.R. Bajpai, S.D. Samant, The enhanced activity of Sb after supporting on K10 in the benzylation of benzene using benzyl chloride and benzyl alcohol, Applied Catalysis A: General, 209 (2001) 229-235.

[37] C.R. Kumar, P.S.S. Prasad, N. Lingaiah, Heteropoly tungstate supported on tin oxide catalysts for liquid phase benzylation of anisole with benzyl alcohol, Applied Catalysis A: General, 384 (2010) 101-106.

[38] A. Ramanathan, H. Zhu, R. Maheswari, B. Subramaniam, Novel zirconium containing cage type silicate (Zr-KIT-5): An efficient Friedel–Crafts alkylation catalyst, Chemical Engineering Journal, 278 (2015) 113-121.

[39] J. Rockenberger, U. zum Felde, M. Tischer, L. Tröger, M. Haase, H. Weller, Near edge X-ray absorption fine structure measurements (XANES) and extended X-ray absorption fine structure measurements (EXAFS) of the valence state and coordination of antimony in doped nanocrystalline SnO_2, The Journal of Chemical Physics, 112 (2000) 4296-4304.

[40] T. Pauporté, Y. Soldo-Olivier, R. Faure, XAS Study of Amorphous WO_3 Formation from a Peroxo-Tungstate Solution, The Journal of Physical Chemistry B, 107 (2003) 8861-8867.

[41] L.A. Morton, M. Miao, T.M. Callaway, T. Chen, S.-J. Chen, A.A. Tuinman, X. Yu, Z. Lu, Z.-L. Xue, Reactions of d^0 tungsten alkylidyne complexes with O_2 or H_2O. Formation of an oxo siloxy complex through unusual silyl migrations, Chemical Communications, 49 (2013) 9555-9557.

[42] Y. Bouhoute, D. Grekov, K.C. Szeto, N. Merle, A. De Mallmann, F. Lefebvre, G. Raffa, I. Del Rosal, L. Maron, R.M. Gauvin, L. Delevoye, M. Taoufik, Accessing Realistic Models for the

WO_3–SiO_2 Industrial Catalyst through the Design of Organometallic Precursors, ACS Catalysis, 6 (2016) 1-18.

[43] G. Chen, M. Dong, J. Li, Z. Wu, G. Wang, Z. Qin, J. Wang, W. Fan, Self-metathesis of 1-butene to propene over SBA-15-supported WO_3, Catalysis Science & Technology, 6 (2016) 5515-5525.

[44] X.-L. Yang, W.-L. Dai, R. Gao, K. Fan, Characterization and catalytic behavior of highly active tungsten-doped SBA-15 catalyst in the synthesis of glutaraldehyde using an anhydrous approach, Journal of Catalysis, 249 (2007) 278-288.

[45] T.Y. Kim, D.S. Park, Y. Choi, J. Baek, J.R. Park, J. Yi, Preparation and characterization of mesoporous Zr-WO_x/SiO_2 catalysts for the esterification of 1-butanol with acetic acid, Journal of Materials Chemistry, 22 (2012) 10021-10028.

[46] H. Shao, M. Huang, H. Fu, S. Wang, L. Wang, J. Lu, Y. Wang, K. Yu, Hollow WO_3/SnO_2 Hetero-Nanofibers: Controlled Synthesis and High Efficiency of Acetone Vapor Detection, Frontiers in Chemistry, 7 (2019) 785.

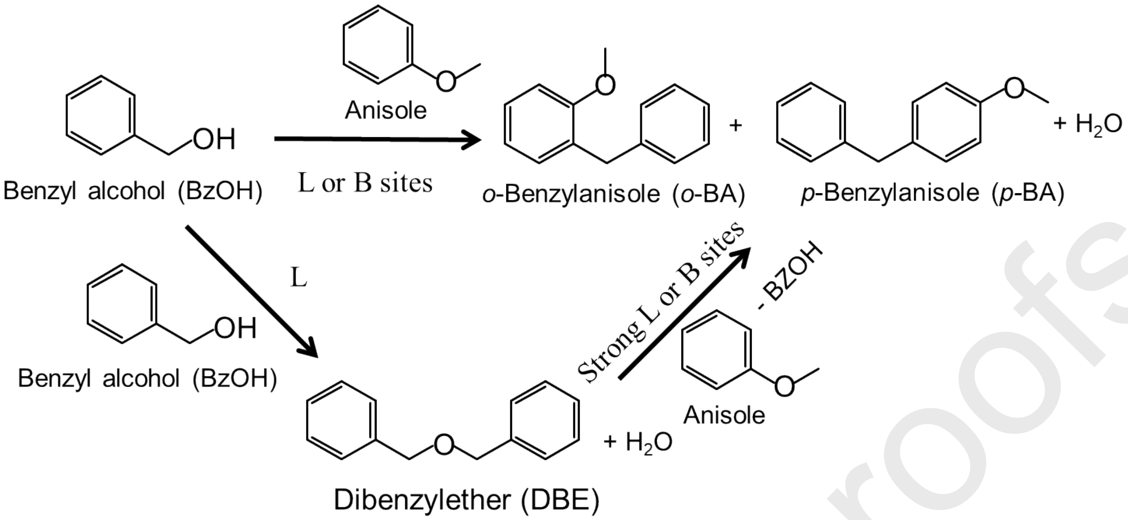

Scheme 1. Influence of acid sites on product selectivity during benzylation of anisole with benzyl alcohol

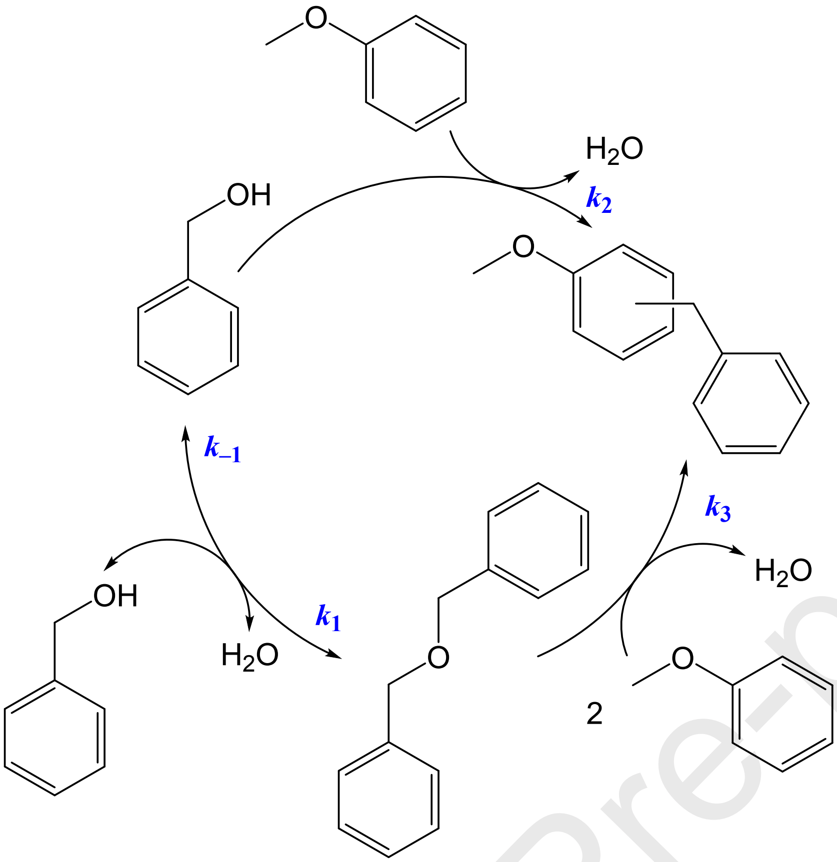

Scheme 2. The scheme of reaction pathways fit best to the kinetic data

Table 1. Metal content, textural properties and total acidity of W_xSn_y samples

Catalyst	M,[b] wt %		Mole ratio		S_{BET}[c]	$V_{p,\ BJH}$[d]	$d_{P,\ BJH}$[e]	Total acidity[f]	L/B
(W_xSn_y)[a]	W	Sn	SiO_2/WO_3	SiO_2/SnO_2	m^2/g	cm^3/g	nm	NH_3 mmol/g	ratio[g]
W_3Sn_5	3.5	4.3	79	41	712	0.98	9.2	0.09	∞
W_9Sn_5	9.2	5.3	27	30	641	0.81	9.2	0.23	11.5
$W_{14}Sn_5$	13.9	5.0	17	30	585	0.73	9.2	0.50	3.8
$W_{23}Sn_5$	23.0	5.4	9	23	411	0.51	11.8	0.56	1.7
$W_{14}Sn_0$	14.0	-	18	-				0.31	3.4
W_0Sn_5	-	5.5	-	33				0.04	∞
W_0Sn_0			-	-	1013	1.30	9.3	0.03	-

[a] x and y represents wt% of Wand Sn; [b] actual elemental wt% measured by XRF; [c] S_{BET} = Specific Surface Area; [d] $V_{P,\ BJH}$ = Total Pore Volume measured at P/P_o= 0.99; [e] $d_{P,BJH}$ = BJH adsorption Pore Diameter; [f] Estimated from NH_3-TPD. [g] Calculated from relative peak areas corresponding to Lewis (L) and Brønsted (B) acid sites, using published adsorption coefficients (0.165 cm $\mu mol^{-1}$for Lewis and 0.078 cm μmol^{-1} for Brønsted acid sites) [24].

Table 2. Comparison of anisole benzylation activity for W_xSn_y catalysts (Reaction conditions: anisole = 100 mmol, BzOH = 10 mmol, dodecane = 2 mmol, T = 130 °C, 1000 rpm)

Entry	Catalyst	t, min	X_{BzOH}	Selectivity (%)			TOF [a]	TOF [b]
				o-BA	*p*-BA	DBE	min^{-1}	min^{-1}
1	None	360	0	–	–	–	0	0
2	W_0Sn_5	120	8.2	-	-	95.1	0.14	
3	W_3Sn_5	120	29.2	30.9	26.9	40.9	0.26	0.74
4	W_9Sn_5	20	42.8	35.3	31.0	33.7	2.46	4.67
		60	97.2	37.7	37.3	24.9		
		120	100	42.1	43.4	14.3		
5	$W_{14}Sn_5$	10	89.6	39.1	37.3	23.6	11.07	17.24
		30	100	48.7	49.2	0		
6	$W_{14}Sn_0$	20	100	11.4	10.4	78.2	3.53	3.53
		60	100	41.7	44.0	14.1		
7	$W_{23}Sn_5$	10	62.0	38.3	35.0	26.6	3.18	4.34
		60	100	46.3	48.1	5.3		

[a] TOF is defined is given by Eq. 3. [b] TOF calculated based on W only.

Table 3. Comparison of anisole benzylation activity for W_xSn_y catalysts with DBE as alkylating agent (Reaction conditions: anisole = 100 mmol, DBE = 5 mmol, dodecane = 2 mmol, T = 130 °C, 1000 rpm)

Entry	Catalyst	t, min	X_{DBE}	Selectivity (%)		TOF[a]
				o-BA	*p*-BA	min^{-1}
1	$W_{14}Sn_0$	10	21.3	52.9	47.1	1.63
		120	91.1	48.8	50.9	
2	W_9Sn_5	20	24.2	54.5	45.5	0.62
		120	88.2	50.4	49.6	
3	$W_{14}Sn_5$	5	22.4	56.5	43.5	1.96
		40	100	51.4	48.3	
4	$W_{23}Sn_5$	5	11.8	58.8	41.2	0.59
		40	93.3	50.7	49.1	

[a] TOF is given by Eq. 3.

Table 4. Rate constants estimated from the kinetic data using model in Scheme 2

Catalyst	W, mmol	Sn, mmol	k_1 [a]	k_{2o} [b]	k_{3o} [b]	k_{2p} [b]	k_{3p} [b]	k_{-1} [b]
$W_{23}Sn_5$	0.125	0.045	5.02	5.26	4.25	6.07	4.78	–
$W_{14}Sn_5$	0.076	0.042	2.76	3.77	3.35	4.45	3.76	–
W_9Sn_5	0.050	0.045	1.88	2.21	1.33	2.65	1.56	1.50
W_3Sn_5	0.019	0.036	0.51	0.64	0.43	0.73	0.49	0.77
$W_{23}Sn_0$	0.130	–	4.11	4.85	3.92	5.88	4.50	–
$W_{14}Sn_0$	0.076	–	2.18	3.27	1.70	3.85	1.92	1.29
W_9Sn_0	0.049	–	1.17	1.71	0.68	2.03	0.88	0.74
W_3Sn_0	0.019	–	–	–	–	–	–	–

Units: [a] for k_1: 10^{-3} L mol^{-1} min^{-1}, [b] for k_{-1}, k_{2o}, k_{2p}, k_{3o}, k_{3p} 10^{-3} min^{-1}

Reaction conditions: catalyst = 100 mg, anisole = 100 mmol, DBE = 5 mmol, dodecane = 2 mmol, T = 110 °C, stirring rate = 1000 rpm

The subscripts o and p in k_2 and k_3 indicate reactions forming *ortho*- and *para*- benzylanisole, respectively. Average relative deviation of predicted concentrations from the experimental ones $\sigma = 0.013 – 0.015$, except $\sigma = 0.040$ for $W_{23}Sn_0$.

Table 5. The results of least-square fits in the *r-space for* W_0Sn_5, $W_{14}Sn_0$ and $W_{14}Sn_5$ samples

Catalyst		CN	Distance (Å)	SS
W_0Sn_5	Sn-O (first shell)	6.24±0.42	2.04±0.01	0.003399
	Sn-O-Snα (second shell)	1.74±0.43	3.15±0.02	0.003399
	Sn-O-Snβ (second shell)	5.44±1.09	3.89±0.01	0.003399
$W_{14}Sn_0$	W-O	4.20±1.38	1.80±0.28	0.01548
	W-O	1.17±0.27	2.41±0.09	0.01548
	W-O-Si	4.93±1.21	3.38±0.05	0.01548
	W-O-W	3.40±1.80	3.82±0.06	0.01548
$W_{14}Sn_5$	Sn-O	6.00±0.42	2.04±0.01	0.004130
	Sn-O-Snα	0.92±0.41	3.16±0.05	0.004130
	Sn-O-Snβ	6.07±1.90	3.97±0.02	0.004130
$W_{14}Sn_5$	W-O	4.35±0.90	1.75±0.02	0.01164
	W-O-Si	2.25±0.82	3.57±0.03	0.00338
	W-O-Sn	3.60±1.03	3.59±0.04	0.00338

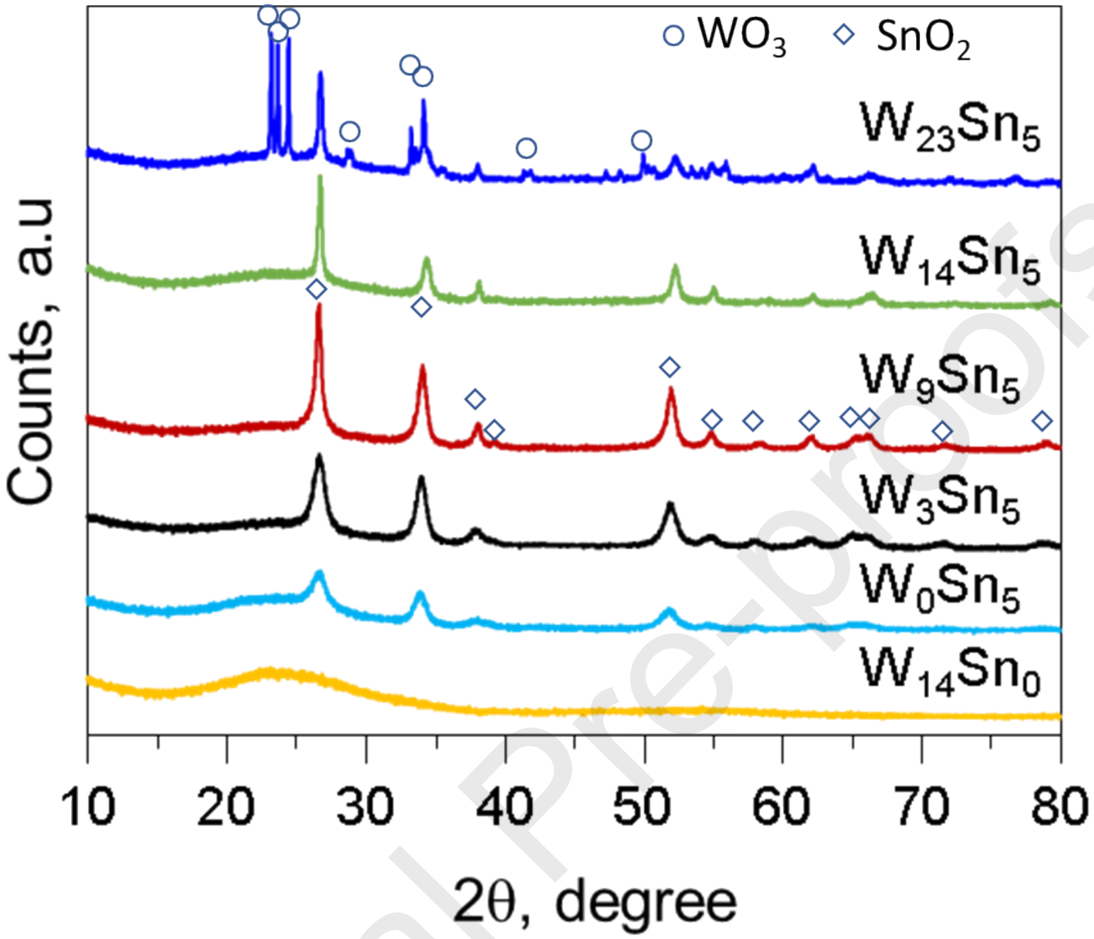

Figure 1. Wide angle XRD patterns of W_xSn_y samples

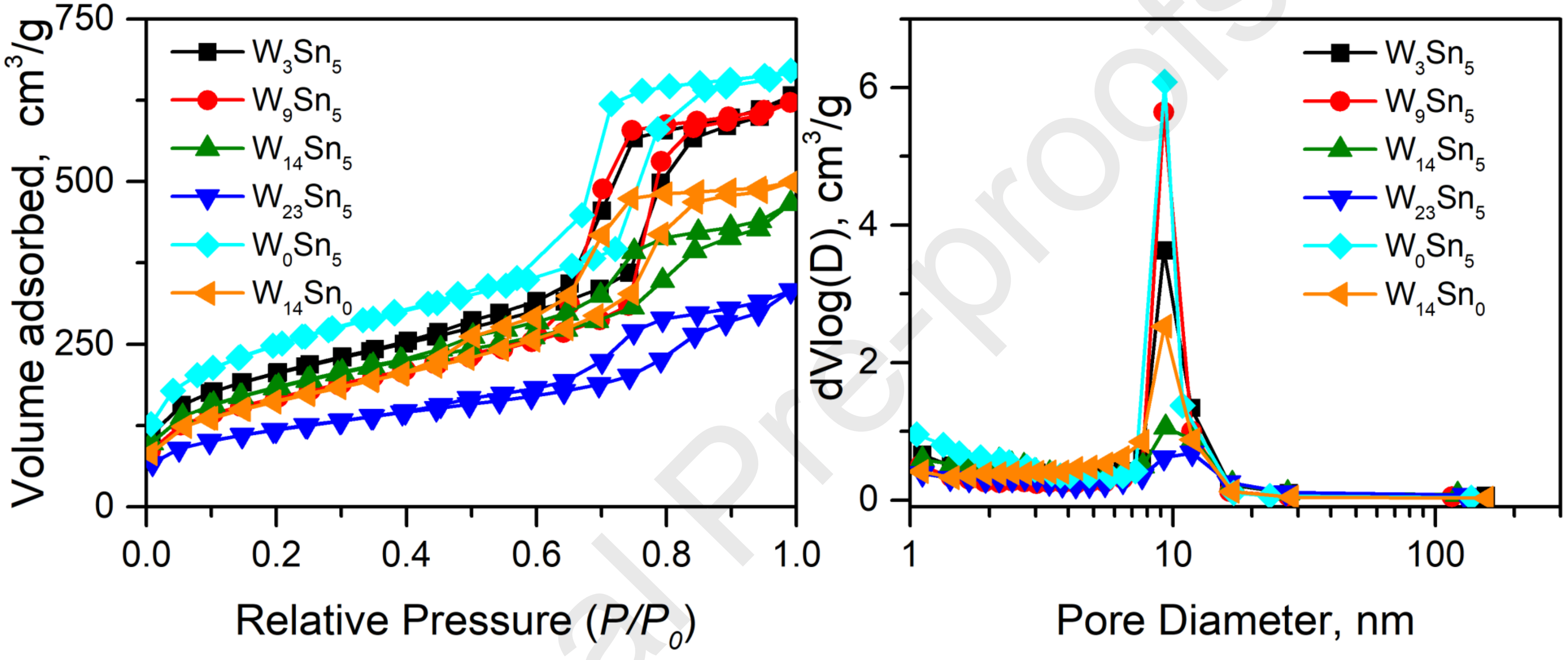

Figure 2. N_2 sorption isotherms and pore size distribution of W_xSn_y samples

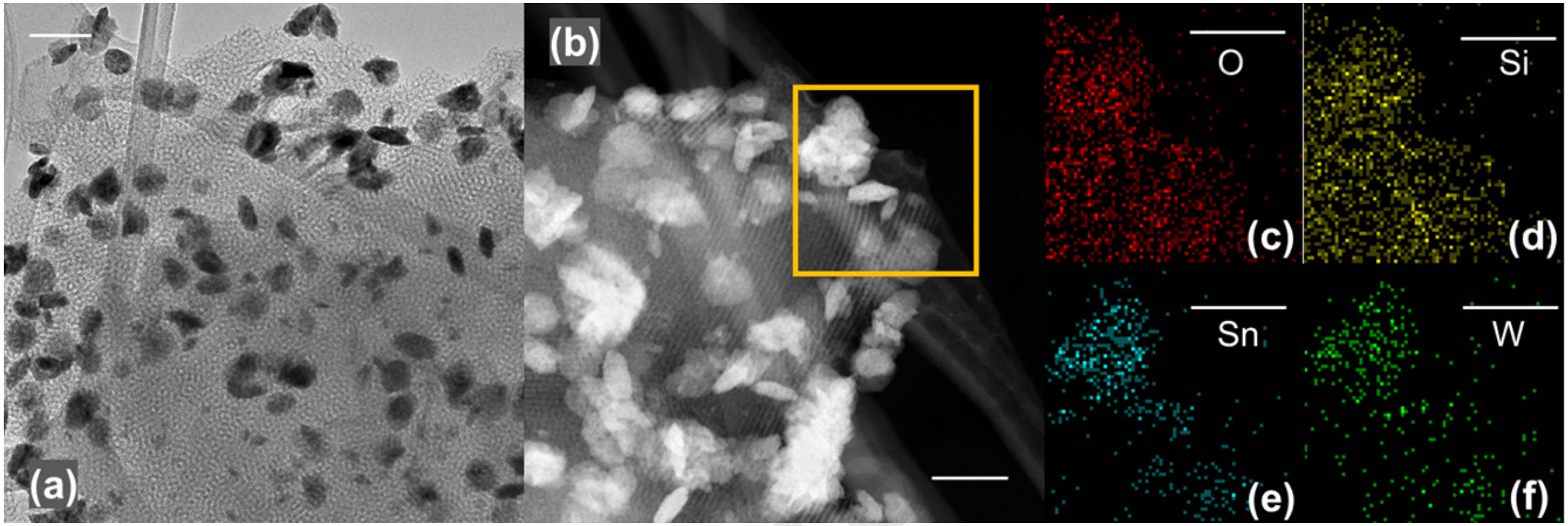

Figure 3. (a)Transmission electron microscopy (TEM) images, (b) STEM image and elemental mapping showing the distribution of (c) O, (d) Si, (e) Sn and (f) W of $W_{14}Sn_5$ sample. The scale bar represents 100 nm.

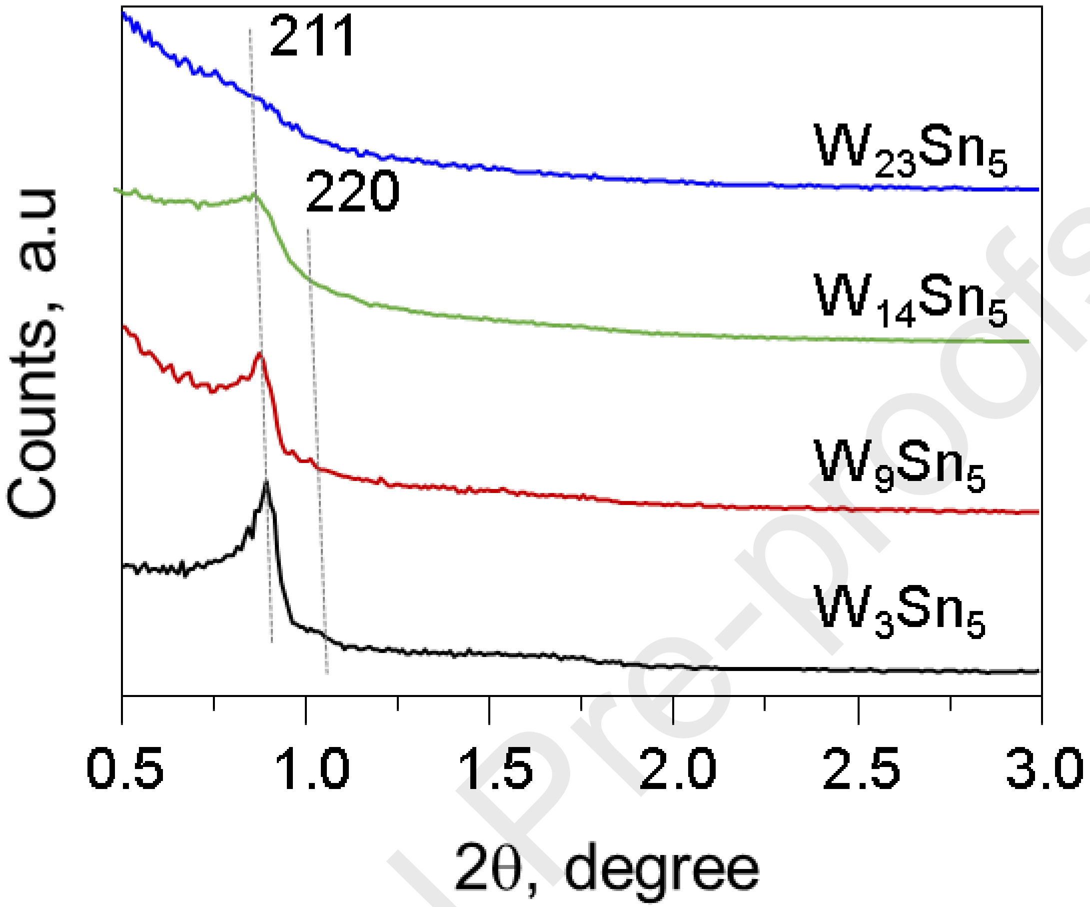

Figure 4. Small angle X-ray scattering patterns of W_xSn_5 samples

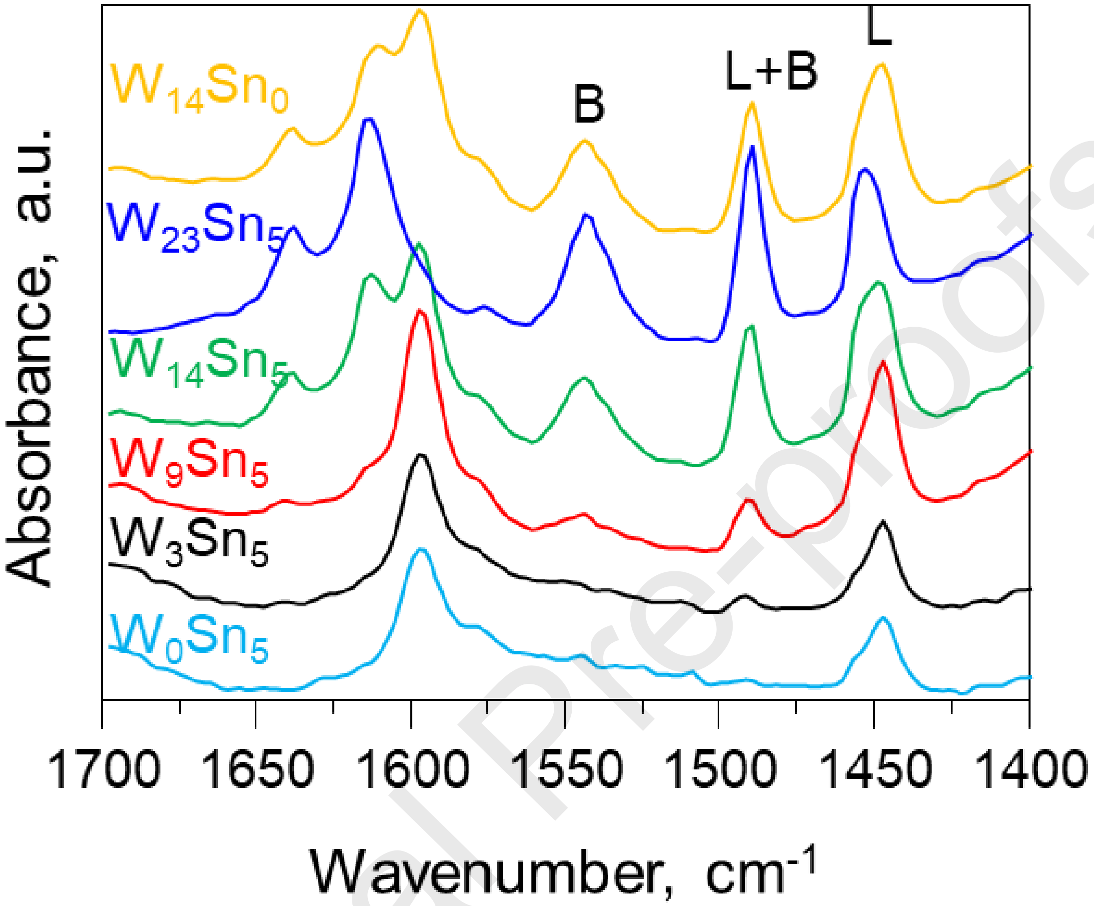

Figure 5. FTIR spectra of adsorbed pyridine over W_xSn_y samples measured at 100 °C.

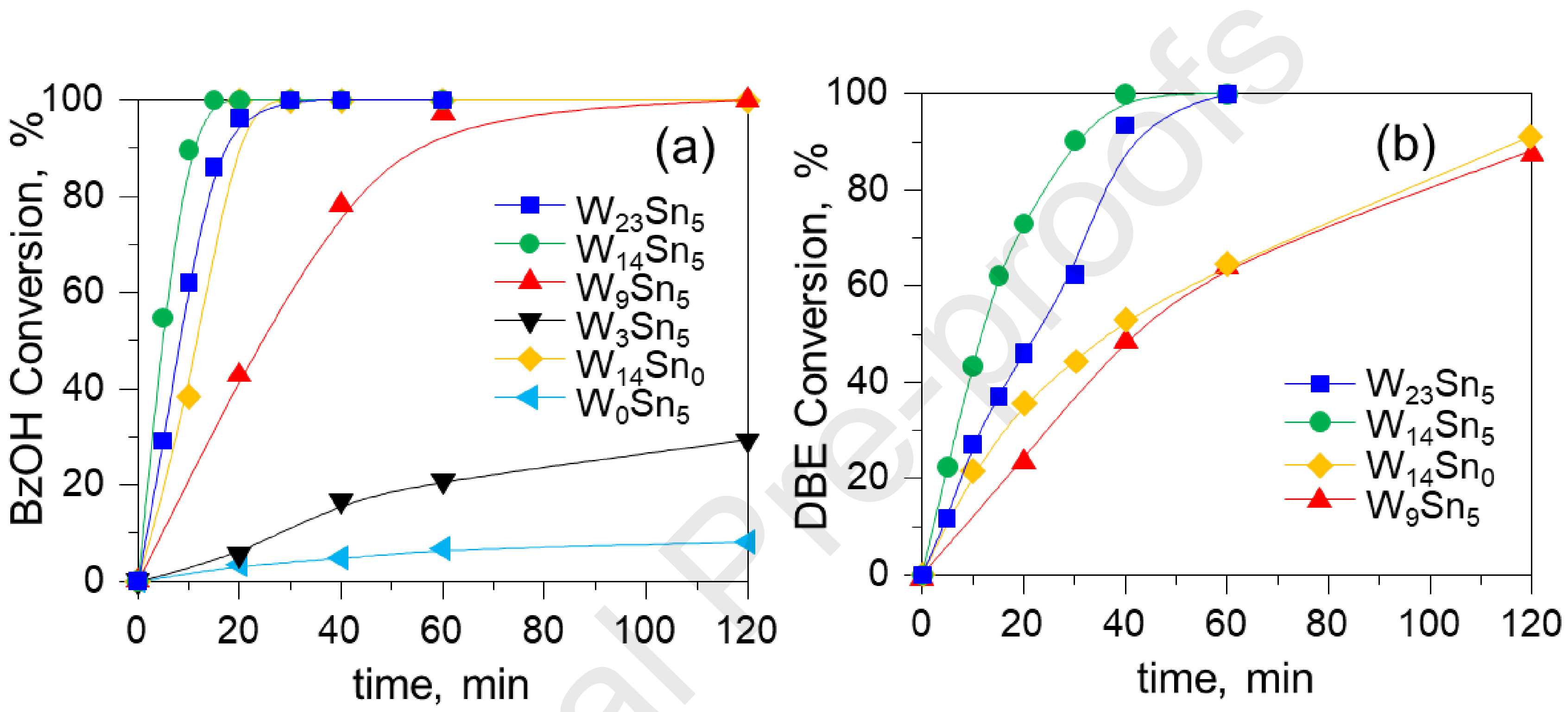

Figure 6. Temporal conversion profiles for anisole benzylation on W_xSn_y catalysts with (a) benzyl alcohol (BzOH); and (b) dibenzyl ether (DBE). Reaction conditions: anisole = 100 mmol, BzOH = 10 mmol or DBE = 5 mmol, dodecane = 2 mmol, T = 130 °C, 1000 rpm

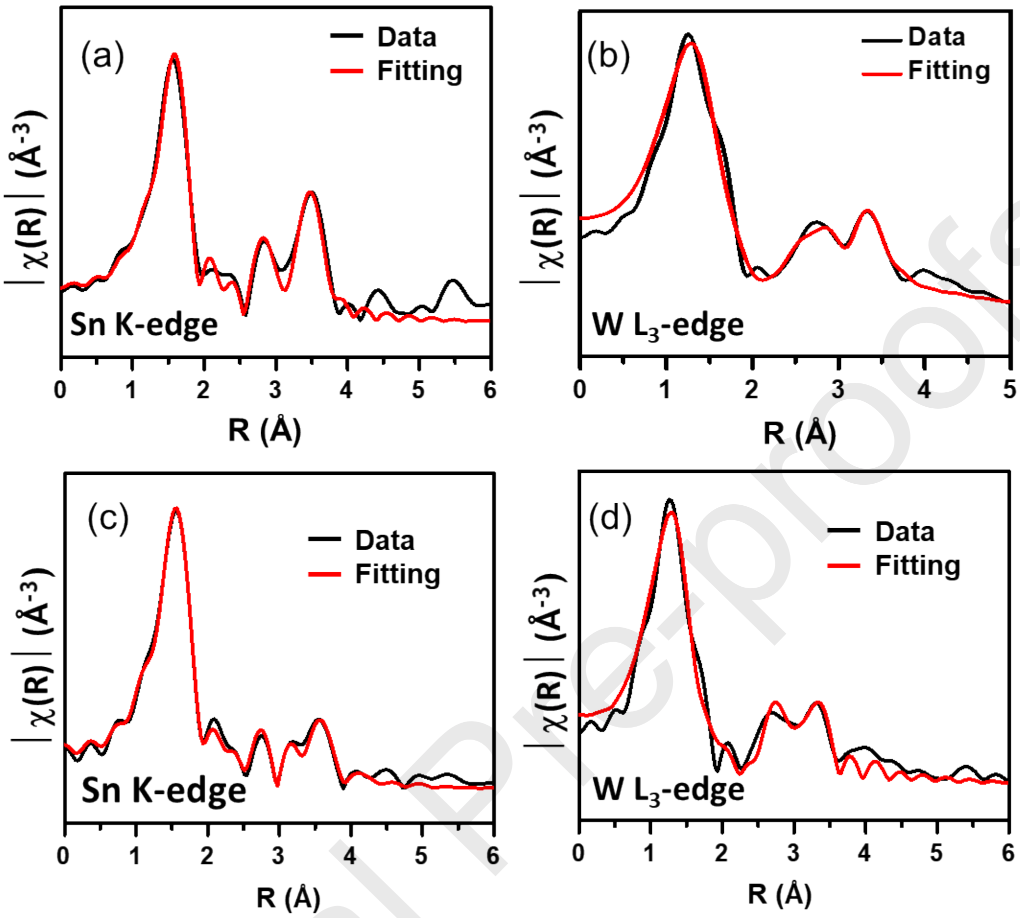

Figure 7. (a) Sn K edge *r*-space data for used W_0Sn_5 sample, (b) W L_3 edge *r*-space data for used $W_{14}Sn_0$ sample and (c and d) *r*-space Sn K and W L_3 edges for used $W_{14}Sn_5$ sample.

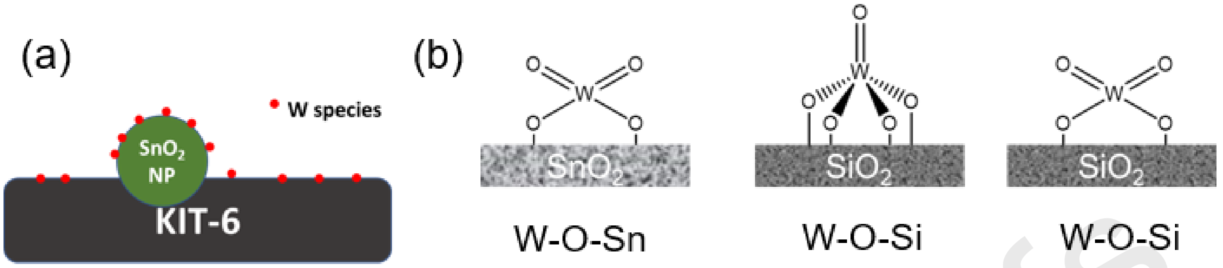

Figure 8(a) A catalyst model for WSn-KIT-6 catalyst. (b) Probable geometries of tungsten coordination with SiO_2 and SnO_2 based on EXAFS studies

Graphical Abstract

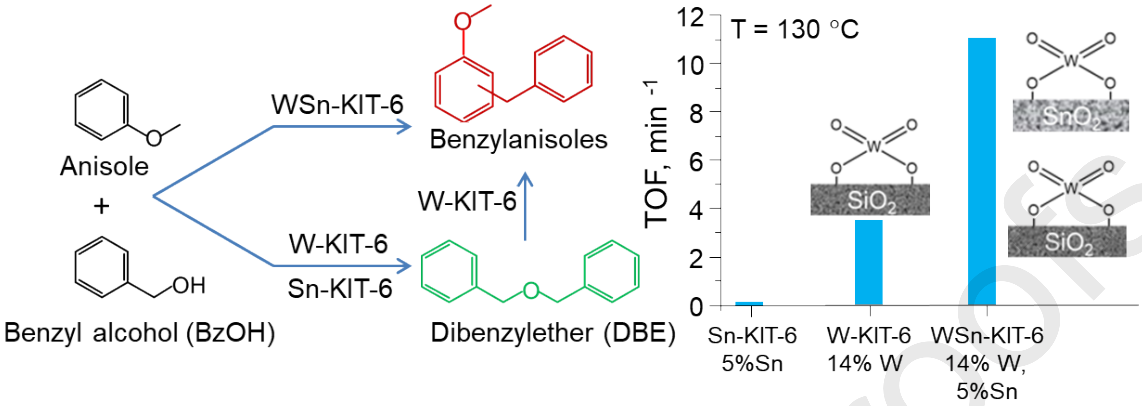

Highlights

- Sn doping of W in KIT-6 demonstrated via sequential addition in a one-pot method
- Uniform WO_x dispersion achieved up to 14% W loading in WSn-KIT-6 catalysts
- WO_x and SnO_x interaction evidenced from H_2-TPR, EXAFS and XPS results
- Anisole benzylation activity correlates mainly with Lewis acid sites
- Intrinsic rate constants are higher for W+Sn catalysts than W-only catalysts

Declaration of interests

☒ The authors declare that they have no known competing financial interests or personal relationships that could have appeared to influence the work reported in this paper.

☐The authors declare the following financial interests/personal relationships which may be considered as potential competing interests: